

ACCEPTED MANUSCRIPT

Modeling Non-Equilibrium Discharge and Validating Transient Plasma Characteristics at Above-Atmospheric Pressure

To cite this article before publication: Riccardo Scarcelli *et al* 2018 *Plasma Sources Sci. Technol.* in press <https://doi.org/10.1088/1361-6595/aaf539>

Manuscript version: Accepted Manuscript

Accepted Manuscript is “the version of the article accepted for publication including all changes made as a result of the peer review process, and which may also include the addition to the article by IOP Publishing of a header, an article ID, a cover sheet and/or an ‘Accepted Manuscript’ watermark, but excluding any other editing, typesetting or other changes made by IOP Publishing and/or its licensors”

This Accepted Manuscript is © 2018 IOP Publishing Ltd.

During the embargo period (the 12 month period from the publication of the Version of Record of this article), the Accepted Manuscript is fully protected by copyright and cannot be reused or reposted elsewhere.

As the Version of Record of this article is going to be / has been published on a subscription basis, this Accepted Manuscript is available for reuse under a CC BY-NC-ND 3.0 licence after the 12 month embargo period.

After the embargo period, everyone is permitted to use copy and redistribute this article for non-commercial purposes only, provided that they adhere to all the terms of the licence <https://creativecommons.org/licenses/by-nc-nd/3.0>

Although reasonable endeavours have been taken to obtain all necessary permissions from third parties to include their copyrighted content within this article, their full citation and copyright line may not be present in this Accepted Manuscript version. Before using any content from this article, please refer to the Version of Record on IOPscience once published for full citation and copyright details, as permissions will likely be required. All third party content is fully copyright protected, unless specifically stated otherwise in the figure caption in the Version of Record.

View the [article online](#) for updates and enhancements.

1

2

3 Modeling Non-Equilibrium Discharge and Validating Transient Plasma

4 Characteristics at Above-Atmospheric Pressure

5

6 Riccardo Scarcelli, Thomas Wallner, Sibendu Som, Argonne National Laboratory

7 Sayan Biswas, Isaac Ekoto, Sandia National Laboratories

8 Douglas Breden, Anand Karpatne, Esgee Technologies

9 Laxminarayan L. Raja, The University of Texas at Austin

10 Abstract

11 Non-equilibrium plasma generated from positive-pulsed nanosecond electrical discharges into desiccated
12 air is simulated in this paper using a multi-dimensional, multi-physics plasma solver. A pin-to-pin electrode
13 configuration is used with a fixed 5.2 mm gap spacing. Peak pulse voltages range between 10.2 and 22.5 kV.
14 Care is taken to match the exact electrode profile from the experiments, and adjust the electron collision
15 frequency so that breakdown limits closely match those from corresponding experimental results. The
16 optimized numerical simulations predict qualitative streamer structure that is in close agreement with
17 experimental observations. Quantitative measurements of atomic oxygen at the anode tip and qualitative
18 estimates of streamer gas heating are closely matched by simulations. The model results are used to provide
19 insight into the spatial and temporal development of the transient plasma. The work performed in this paper
20 delivers a numerical tool that can be extremely useful to link the post-discharge plasma properties to low-
21 temperature plasma ignition mechanisms that are of great interest for the automotive industry.

22 Introduction

23 Following the technological development of spark-ignition (SI) internal combustion engines (ICEs),
24 non-conventional ignition technologies are being increasingly considered as a potential replacement for
25 conventional inductive or capacitive spark-based ignition systems [1]. Among those technologies, low-
26 temperature plasma (LTP), also known as non-equilibrium plasma, attracts the highest interest from
27 automotive OEMs due to promising performance [2,3] and lack of significant technological barriers
28 affecting the operation of other ignition systems (e.g. the lens fouling issue generated by laser systems). In
29 particular, LTP does not induce significant heating at the electrode surface, which helps to increase the
30 ignition hardware lifetime and reduce the ignition energy lost through heat transfer.

31 Research on plasma assisted ignition and combustion (PAI/PAC) has been intensively carried out for more
32 than a decade [4,5]. Nevertheless, the application of LTP to engine ignition processes is still very novel.
33 Most of the existing literature on LTP modeling focuses on low-pressure applications [5], where the plasma

characteristics are fairly uniform in space, and 0-D chemistry solvers can trace the evolution of the most relevant chemical species (including electrons, ions, radicals, atoms, and molecules, in their ground or excited state) with relatively short computational run times. However, engine applications are characterized by above-atmospheric pressures and temperatures, especially in a PAI mode. As a result, generated plasma streamers are non-uniform, with a broad distribution of chemical and thermal properties. Within the engine research community, a number of PAI systems have been investigated including microwaves [6,7], radio-frequency (RF) discharges [8,9], and nanosecond pulsed discharges [10,11]. The nanosecond pulsed discharge, or transient plasma, is of particular interest because of its potential for higher reduced electric field (E/N) values with respect to microwaves or RF discharges. Higher E/N leads to higher ionization and dissociation rates with lower energy utilization rates.

Pai et al. [12] parametrically studied repetitively pulsed nanosecond discharges in air at atmospheric pressure, and have confirmed the existence of three distinctive regimes, namely the corona, glow, and spark regimes. The spark regime introduces substantial gas heating and generates a high-current, luminous electrical arc. Electrical energy for the arcing discharges in the spark regime is more efficiently converted into thermal energy that results in electrode surface erosion. Both corona and glow regimes are non-thermal discharges. The glow regime occupies a larger spatial region across the discharge gap, while the corona regime is limited to the vicinity of the anode. The more diffuse glow regime is thus attractive for advanced ignition systems. Recently, Wolk and Ekoto have presented experimental observations of single- and multi-pulse nanosecond discharges in air at room temperature and pressure values from 1 bar to 9 bar [13,14]. They focused their research on identifying the mechanism for transition from glow to spark regime in a multi-pulse discharge. Also, they characterized the transition from glow to spark regime for a single-pulse discharge. Finally, they provided qualitative analysis of the distribution of atomic oxygen (excited state) and temperature in the glow phase, using direct imaging and schlieren technique respectively.

As of today, computational fluid dynamics (CFD) tools used for ICE multi-dimensional simulations do not offer LTP ignition models. The LTP ignition mechanism is quite different from the conventional, thermal ignition mechanism. In the former, ignition is triggered by the increase of the concentration of active species such as radicals, ions, and excited molecules rather than local high temperature values [15]. As an example, atomic oxygen (O) has been experimentally identified as a product of nanosecond pulsed discharge, which also features long enough lifetime to influence hydrocarbon combustion reactions [11]. Overall, state-of-the-art ignition models implemented in engine CFD solvers cannot be used to describe LTP ignition mechanism, and new conceptual models need to be developed. To this aim, the key question concerns the characteristics of the plasma at the end of the electrical discharge. It is known that in a transient plasma there can be significant non-equilibrium in the species composition, with a large disparity in the electron

temperature that can be much higher than the translational temperature of the heavier species in the plasma. In addition, other degrees of freedom in the plasma such as vibrationally excited molecules can exist that are themselves characterized by different temperatures from the electron and heavy species translational temperatures. This complicates the description of combustion chemistry that has traditionally relied on a temperature single-value assumption for determining species production/destruction rates. From a combustion modeling perspective, when using the Arrhenius correlation for the reaction rate, the key information that is needed includes temperature and concentration of the reactants. At above-atmospheric conditions, these quantities are not uniform in space.

Multi-dimensional LTP modeling has been recently performed in a detailed fashion, although for very simple geometries. Among the most significant contributions that can be found in literature, Tholin and Bourdon performed a series of numerical studies [16,17] on the glow regime of repetitively pulsed nanosecond discharge from two pin electrodes in atmospheric air, which are in direct comparison with the experimental studies of Pai et al [12]. They have analyzed the streamer characteristics in terms of propagation speed and the conditions for transitions into the spark or corona regimes. Furthermore, they have mimicked the multi-pulse behavior of the non-equilibrium discharge and investigated the conditions for the plasma to remain in a glow phase. Recently, the authors of this paper have conducted initial LTP multi-dimensional simulation studies [18] based on the experiments carried out by Wolk and Ekoto [14]. The electrode geometry and gap spacing were matched to the experiment, with the measured voltage signal used as the simulation input boundary condition. Predicted distributions of local gas heating and chemically reactive species like atomic oxygen were successfully compared to qualitative images of temperature gradients using the schlieren technique and electronically excited states of atomic oxygen using direct imaging. Also, the LTP transition into the spark regime (i.e. arcing condition) was mapped out as a function of initial pressure, with the results compared to the experiments. Overall, the model showed good accuracy, although the transition pressure was not perfectly matched by the simulations.

This paper expands our previous research efforts and has two main objectives: 1) reduce or eliminate the discrepancy between modeling and experiments in terms of LTP-to-arc transition pressure; 2) provide a quantitative validation of the plasma thermal and chemical characteristics. To this aim, better control on the gas composition, geometry of the electrodes, and voltage measurements was achieved. Parametric simulations were performed, with model constants tuned to match the experiments. Finally, the quantitative comparison of relevant quantities such as temperature and atomic oxygen concentration, between simulations and experiments, was carried out at the same location.

Experimental setup and conditions

The experimental apparatus was previously discussed in detail by Wolk and Ekoto [13,14], therefore only a brief description is presented here. All experiments were performed in a stainless steel 316 custom-built, optically accessible, spark calorimeter with an internal volume of 29 cm³. During the experiment, the initial calorimeter temperature, $T_{initial}$, was heated to a temperature of 70 °C (343 K) using resistive heating tape with the temperature monitored using embedded K-type thermocouples. The calorimeter was filled up to the desired pressure (up to 3.4 bar absolute, for this case) using desiccated air with 20.95% O₂ by volume. Key specifications and operating conditions of the calorimeter are reported in Table 1. To generate the pulse nanosecond discharges within the calorimeter, a Transient Plasma Systems Inc. SSPG-101-HF high-voltage (28 kV peak) pulse generator with a 12-ns full width at half max (FWHM) pulse width and a 5 ns rise time was used. A low-impedance inline attenuator was used to monitor pulse voltage and current for each discharge event.

Table 1. Calorimeter specifications and operating conditions.

Internal volume (cm ³)	29
Distance between electrodes (mm)	5.2
Initial temperature (°C)	70
Initial pressure (bar)	1.2 – 3.4
Voltage (kV)	10.3 – 22.5
Mixture composition (% volume)	20.95% O ₂ , 79.05% N ₂

The relative position of the anode and cathode is schematically shown in Figure 1. The high-voltage anode was built by modifying an NGK DP7EA-9 size M12 non-resistive spark plug. The plug J-hook and top 1 cm of the outer body ground were removed, with the anode tip machined to a rounded point (~ 125 µm radius of curvature) to maximize the local electric field strengths, while maintaining relatively repeatable discharge characteristics. The anode was centrally positioned at the top of the calorimeter. A sharpened 3.18 mm diameter stainless steel rod was used as the cathode. The cathode was installed from the calorimeter base and secured in place by a Swagelok fitting. A constant inter-electrode distance of 5.2 mm was maintained throughout for the present study. It is worth noting that, different from the anode, the cathode has a flat top circular tip and the dimension ($\phi = 0.44$ mm) was measured experimentally. Figure 1 also shows the location (0.1 mm below the anode tip) and size (0.5 mm diameter) of the domain used for O-TALIF measurement of the atomic oxygen (ground state) concentration. Simulations results were probed at the same location/size.

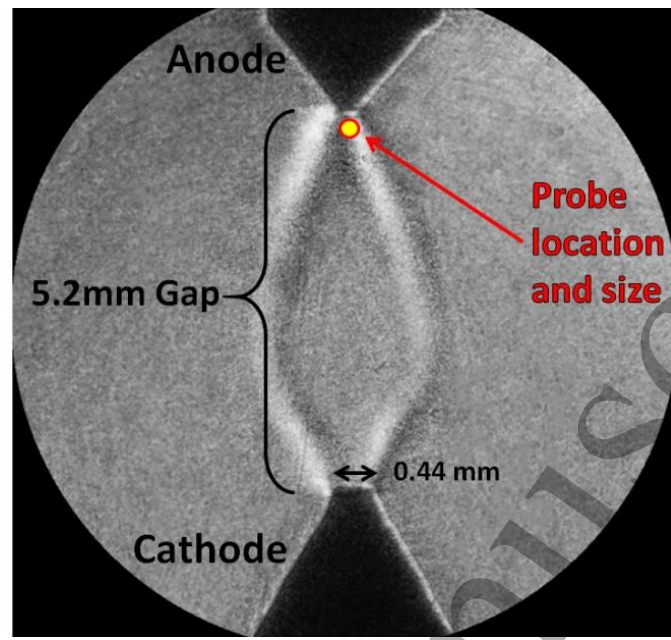


Figure 1 Detail of electrodes position and location of the probe for experimental sampling

The experimental conditions evaluated for model validation are listed in Table 2. These conditions explored the LTP characteristics, just above the pressure threshold that identifies the transition from spark (arc) to glow (LTP) regime, when the peak voltage was varied between 10.3 kV and 22.5 kV. The corresponding initial pressure was varied between 1.2 bar and 3.4 bar absolute with initial temperature fixed at 70 °C. For these conditions, the chamber gas densities were similar to the densities encountered in a naturally aspirated engine for very early spark timings [2]. The above-arc pressure value shown in Table 2 represents the lowest value of initial pressure that is needed to completely avoid spark.

Table 2. Experimental conditions evaluated for model validation

#	Voltage (kV)	Above-arc absolute pressure (bar)
1	10.3	1.2
2	14.4	1.5
3	19.2	2.0
4	22.5	3.4

Measured profiles of voltage are plotted in Figure 2. The assumption made in simulations, which is also verified by experiments, is that the voltage profile does not change even if the initial pressure changes unless an arc event (plasma in the spark regime) is detected. Also, only the main pulse is simulated, since the subsequent voltage oscillations (also referred as to ringing) have a relatively lower impact. This assumption will be discussed later in the paper.

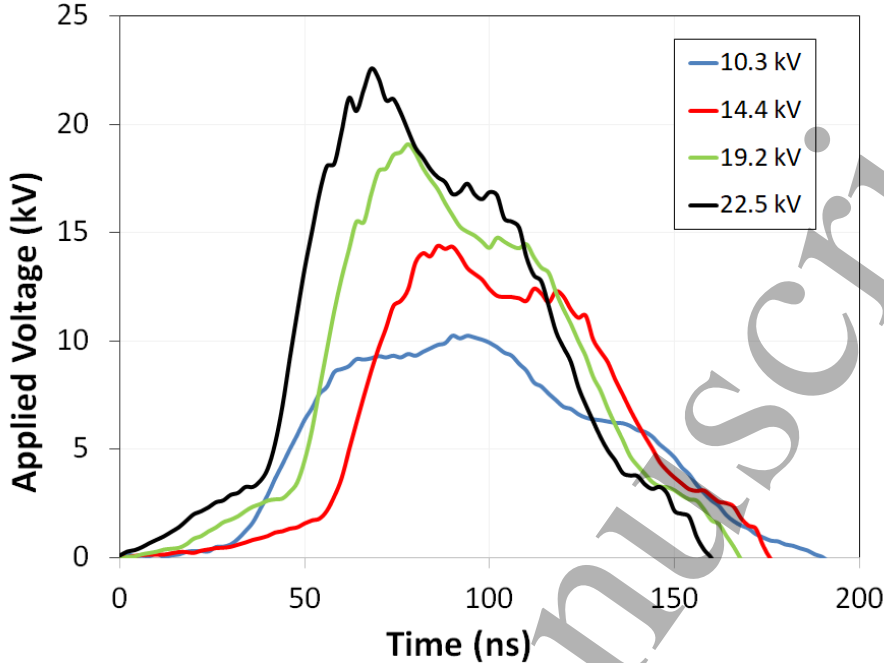


Figure 2. Voltage profile traces measured in experiments and used as boundary conditions for transient plasma simulations

Numerical model setup

Plasma modeling

The transient plasma simulations performed in this paper are carried out using the commercial non-equilibrium plasma solver VizGlow, version 2.1 [19]. VizGlow is a general purpose self-consistent, multi-species, multi-temperature plasma solver developed by Esgee Technologies Inc., which can be specialized to describe the high-pressure streamer as well as corona discharge [20]. Poisson's equation is solved for the self-consistent electrostatic field in the plasma. In addition, a number of differential equations are solved that account for the production/destruction and transport of multiple charged and neutral species along with the electron and bulk gas energy distribution. The model also accounts for the photoionization process which is an important source of background electrons for the streamer propagation in air mixtures, in particular for streamers generated from positive electrodes (also referred as to positive streamers).

Species continuity equation is formulated as follows:

$$\frac{\partial n_k}{\partial t} + \vec{\nabla} \cdot \vec{r}_k = \dot{G}_k \quad \text{Equation 1}$$

where k is the species index. All involved species are solved for except for the dominant background neutral species. The number density of the dominant background species is calculated from the ideal gas law at a

specified total gas pressure and gas temperature, by subtracting all other species. The gas chemistry source term, \dot{G}_k , is calculated using a finite-rate chemistry mechanism.

The species number flux term $\vec{\Gamma}_k$ is obtained using the drift-diffusion approximation formulated below:

$$\vec{\Gamma}_k = n_k \vec{u}_k = \mu_k n_k \vec{E} - D_k \vec{\nabla} n_k \quad \text{Equation 2}$$

The drift-diffusion approximation is accurate at pressures of 100 mTorr and higher and at room temperature when the mean free path of the species (on order of μm) are much smaller than the characteristics length scales of the geometry (on order of mm).

The electrostatic potential ϕ is calculated by solving Poisson's equation:

$$\nabla^2 \phi = -\frac{e}{\epsilon_0 \epsilon_r} \sum_k Z_k n_k \quad \text{Equation 3}$$

where ϵ_0 is the permittivity of free space, ϵ_r is the relative permittivity of the material, and Z_k is the charge number of the individual species k . The relative permittivity is 1 for the gas domain. The charge number is -1 for electrons, +1 for all singly ionized positive ions and -1 for singly charged negative ions.

Electron energy transport is accounted for by solving the electron temperature using the electron energy conservation equation:

$$\frac{\partial e_e}{\partial t} + \vec{\nabla} \cdot ((e_e + p_e) \vec{u}_e - \kappa_e \vec{\nabla} T_e) = e \vec{\Gamma}_e \cdot \vec{\nabla} \phi - e \sum_i \Delta E_i^e r_i - \frac{3}{2} k_B n_e \frac{2m_e}{m_b} (T_e - T_g) \bar{v}_e \quad \text{Equation 4}$$

The total electron energy is assumed to be approximately equal to the mean electron energy $e_e = \frac{3}{2} k_B n_e T_e$, while the electron pressure p_e is obtained using the ideal gas law. The right-hand side of the electron energy equation incorporates three source terms: Joule heating, inelastic collisional heating, and elastic collisional heating, respectively.

The bulk temperature is obtained by solving the energy conservation equation:

$$\frac{\partial e_h}{\partial t} + \vec{\nabla} \cdot (-\kappa_h \vec{\nabla} T_h) = \sum_k e Z_k \vec{\Gamma}_k \cdot \vec{\nabla} \phi + \frac{3}{2} k_B n_e \frac{2m_e}{m_b} (T_e - T_h) \bar{v}_e - e \sum_i \Delta E_i^h r_i \quad \text{Equation 5}$$

Here bulk energy per unit volume $e_h = C_v T_h$ is assumed to be the same for all heavy species. κ_h is the bulk thermal conductivity. This equation includes the effect of several source terms (shown on the right-hand side). The first source term represents summation of Joule heating over all ion species k . The second term

is a measure of the bulk energy gain due to elastic collisions of between heavy species and electrons. Further, heat loss due to inelastic collisions is calculated by performing a summation over all heavy species reactions. Here, ΔE_i^h is the loss of heavy species energy per collision and r_i is the rate of progress for reaction ‘ i ’. The simulations performed in this study leverage the assumption that the bulk fluid motion is omitted, due to the small temporal scale of the discharge. Therefore, local mean velocity, \vec{u}_h , is equal to zero and does not appear in Equation 5, while pressure is fixed.

In this work, the boundary conditions imposed on this problem are at solid surfaces, the axis line and the outer ambient. At solid walls, the flux of each species to and from the wall is imposed. For every species k , the one-directional temperature dependent Maxwellian flux normal to the wall which can be written as

$$\vec{\Gamma}_k \cdot \hat{n} = \frac{1}{4} n_k \sqrt{\frac{8k_b T_k}{\pi m_k}} \quad \text{Equation 6}$$

Where T_k is the temperature of species k , k_b is Boltzmann’s constant, n_k is the volumetric number density of species k and m_k is the species mass. The unit direction normal into the wall is \hat{n} .

Electrons may be emitted from the wall when other species i impact the wall in a process known as secondary electron emission.

$$\vec{\Gamma}_{e,\text{secondary}} \cdot \hat{n} = - \sum_i \gamma_i \vec{\Gamma}_i \cdot \hat{n} \quad \text{Equation 7}$$

Where the incoming flux of species i is $\vec{\Gamma}_i$, the secondary emission coefficient representing number of electrons emitted per impacting particle i is γ_i and the minus sign indicates that electrons are being emitted away from the wall into the plasma.

For charged ion species, if the product of the electric field and the species charge number is directed towards the wall (indicating bombardment) and additional wall flux term $\vec{\Gamma}_{k,\text{bombardment}}$ is included.

$$\vec{\Gamma}_{k,\text{bombardment}} \cdot \hat{n} = n_k Z_k \vec{E} \cdot \hat{n} \quad \text{if} \quad Z_k \vec{E} \cdot \hat{n} > 0 \quad \text{Equation 8}$$

Electron’s impact the wall each carry an energy of $2k_b T_e$ Joules of energy. For electrons emitted from the wall due to secondary impact, each electron carries with it an energy of $e\Delta E_{e,k}$ Joules. The term $\Delta E_{e,k}$ is the energy in eV that each electron carries with it when it is ejected and is specified as an input.

$$\vec{\Gamma}_e \cdot \hat{n} = 2k_b T_e \frac{1}{4} n_k \sqrt{\frac{8k_b T_k}{\pi m_k}} - \sum_i e\Delta E_{e,k} \gamma_i \vec{\Gamma}_i \cdot \hat{n} \quad \text{Equation 9}$$

At the sides/far field regions symmetric boundary conditions are used. Symmetric boundary condition specify that the value of the conserved variable (electrostatic potential, species densities and energies) are mirrored at the boundary. At axis boundaries, the net flux of species densities and energies are set to zero based on the principle that an axis face has zero area.

The gas-species transport formulation for plasma is implemented in the GASACT species properties and chemistry library that is part of the VizGlow software package [19]. The species diffusion coefficient, D_k , the species mobility (for charged species), μ_k , and the species thermal conductivity, k_k , can be defined in terms of the collision frequency, $\bar{\nu}_{kb}$, as follows:

$$D_k = \frac{k_B T_{k,eff}}{m_k \bar{\nu}_{kb}} \quad \mu_k = \frac{Z_k e}{m_k \bar{\nu}_{kb}} \quad k_k = \frac{5}{2} k_B D_k n_k \quad \text{Equation 10}$$

The transport properties assume a Maxwellian or a near-Maxwellian distribution function for the species. However, especially in the case of electrons, the velocity distribution function can be significantly different from a Maxwellian. VizGlow provides flexibility to nominally correct for these errors. A pre-factor multiplier can be specified for all of the above species transport properties, and in particular for the species collision frequency, as follows:

$$\bar{\nu}_{kb} = \xi_{v_k} \bar{\nu}_{kb,orig} \quad \text{Equation 11}$$

A plasma chemical kinetic mechanism for air (N_2 and O_2) is used in this study. The mechanism consists of a total of 18 species: E, O_2 , O_2^* , O_2a1 , O_2b1 , O_2+ , O_2- , O, O^- , O_4^+ , O_2+N_2 , N_2 , N_{2a1} , N_{2A} , N_{2B} , N_{2C} , N_{2+} , N_{4+} . Here, E is electrons, O_2^* is the excited Herzberg state, O_2a1 is the singlet delta, and O_2b1 is a singlet sigma excited states of molecular oxygen, N_{2a1} , N_{2A} , N_{2B} , and N_{2C} are electronically states of molecular nitrogen, species symbols with “+” indicate positive ions, and “-” indicate negative ions. We also note cluster ions O_4^+ , O_2+N_2 , and N_{4+} that are stable forms. Table II in Ref. [20] provide additional information on these species. The chemistry mechanism comprises reaction rate pathways from the literature [21,22,23] and shown in Table 3.

In Table 3, reactions are either Arrhenius reaction rates or they are generated and tabulated from cross-section data. If a reaction is not labeled BOLSIG+ then it is an Arrhenius reaction rate. The letter A, B and C are terms in the Arrhenius rate coefficient formula given by

$$k = AT^B e^{\frac{-T}{C}} \quad \text{Equation 12}$$

All reactions labelled BOLSIG+ are a function of the electron temperature, T_e , while the reaction rates involving neutrals (given as Arrhenius reaction rates), are a function of a single heavy species temperature, T_g . Electron impact reactions of O₂ and N₂ were generated using the offline Boltzmann solver BOLSIG+ [24] and the cross-sectional data for N₂ and O₂ [22]. While the electron properties, including mobility, were calculated using BOLSIG+, the electron collision frequency multiplier was used in this study as a tuning parameters to account for the general uncertainty that exists in determining the collision cross-section of the electron-impact reactions.

Electron impact reactions with oxygen and nitrogen molecules can lead to several different excited energy states of both short and long life times. In this mechanism, rotational and vibrational excited states are not explicitly tracked, but the loss of electron energy in generating these excited modes is accounted for in the reaction mechanism. Several electronically excited species of nitrogen and oxygen are however explicitly represented as individual species with the corresponding production/destruction pathways in the mechanism.

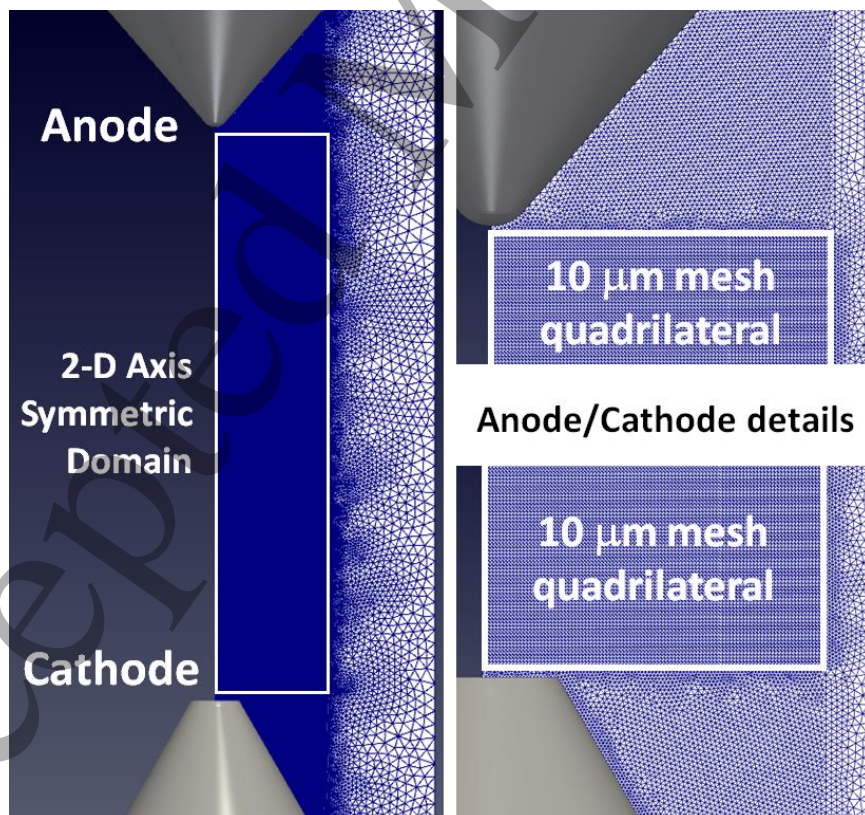
Streamer discharges (in particular positively charged or cathode-directed) require an initial seed electron charge distribution to propagate. An important physical process that provides electron seed charge for the streamer to propagate is photoionizing radiation emitted by the active ionizing zone of the streamer. In this study, we utilize an air photoionization model based on the three-term exponential Helmholtz model described in detail in Bourdon et al. [25] and used in prior numerical studies on streamer discharges for atmospheric pressure plasma jets [26]. The radiation source term for ionization of oxygen due to photoemission from electron impact of nitrogen can be modeled using a volume integral model described by Zheleznyak et al [27]. While the integral model is simple, it must be evaluated for every emission cell/absorption cell pair and can be computational very expensive. The Helmholtz model approximates the full integral which solves three Helmholtz equations for three contributions. The sum of the contributions provides the volumetric photoionizing source term. The three-term Helmholtz model is significantly more efficient from computation standpoint with minimal loss of accuracy [25]. In air, the model assumes that the emission of ionizing photons is proportional to electron impact ionization of nitrogen molecules. The emitted radiation has wavelengths in the range of 98-102.5 nm (~12.1-12.65 eV) which are sufficient to ionize oxygen molecules.

Table 3. Reactions of the plasma detailed mechanism used in this study

Rxn	Reaction	A (molecules-m)	B (non-dim)	C (Kelvin)	$\Delta E_{\text{electron}} (\text{eV})$	$\Delta E_{\text{background}} (\text{eV})$
G ₁	E + N ₂ -> E + N ₂ (rotational)		BOLSIG+		-0.02	0.02
G ₂	E + N ₂ -> E + N ₂ (vibrational)		BOLSIG+		-1.0	1.0
G ₃	E + N ₂ -> E + N ₂ A		BOLSIG+		-6.17	-
G ₄	E + N ₂ -> E + N ₂ B		BOLSIG+		-7.35	-
G ₅	E + N ₂ -> E + N ₂ B		BOLSIG+		-7.36	-
G ₆	E + N ₂ -> E + N ₂ B		BOLSIG+		-8.16	-
G ₇	E + N ₂ -> E + N ₂ a1		BOLSIG+		-8.4	-
G ₈	E + N ₂ -> E + N ₂ a1		BOLSIG+		-8.55	-
G ₉	E + N ₂ -> E + N ₂ a1		BOLSIG+		-8.89	-
G ₁₀	E + N ₂ -> E + N ₂ C		BOLSIG+		-11.03	-
G ₁₁	E + N ₂ -> E + N ₂ (electronic exc.)		BOLSIG+		-11.88	11.88
G ₁₂	E + N ₂ -> E + N ₂ (electronic exc.)		BOLSIG+		-12.25	12.25
G ₁₃	E + N ₂ -> E + N ₂ (electronic exc.)		BOLSIG+		-13.0	13.0
G ₁₄	E + N ₂ -> 2E + N ₂ ⁺		BOLSIG+		-15.6	-
G ₁₅	E + O ₂ -> E + O ₂ (rotational)		BOLSIG+		-0.02	0.02
G ₁₆	E + O ₂ -> E + O ₂ (vibrational)		BOLSIG+		-0.193	0.193
G ₁₇	E + O ₂ -> E + O ₂ a1		BOLSIG+		-0.98	-
G ₁₈	E + O ₂ -> E + O ₂ b1		BOLSIG+		-1.63	-
G ₁₉	E + O ₂ -> E + O ₂ [*]		BOLSIG+		-4.5	-
G ₂₀	E + O ₂ -> E + O ₂ (electronic exc.)		BOLSIG+		-6.0	6.0
G ₂₁	E + O ₂ -> E + O ₂ (electronic exc.)		BOLSIG+		-8.4	8.4
G ₂₂	E + O ₂ -> E + O ₂ (electronic exc.)		BOLSIG+		-9.97	9.97
G ₂₃	E + O ₂ -> E + O + O		BOLSIG+		-5.58	5.58
G ₂₄	E + O ₂ -> E + O + O (electronic exc.)		BOLSIG+		-8.4	8.4
G ₂₅	E + O ₂ -> E + E + O ₂ ⁺		BOLSIG+		-12.07	-
G ₂₆	E + O -> E + O		BOLSIG+		-6.34	6.34
G ₂₇	E + O ₂ ⁺ -> O + O		BOLSIG+		6.91	-
G ₂₈	E + O ₄ ⁺ -> O ₂ + O ₂		BOLSIG+		12.07	-
G ₂₉	E + O ₂ -> O ⁻ + O		BOLSIG+		-4.66	-
G ₃₀	E + O ₂ a1 -> E + O ₂ b1		BOLSIG+		-0.65	-
G ₃₁	E + O ₂ a1 -> E + O + O		BOLSIG+		-6.34	-
G ₃₂	E + O ₂ a1 -> O ⁻ + O		BOLSIG+		-3.9	-
G ₃₃	E + O ₂ b1 -> O ⁻ + O		BOLSIG+		-3.7	-
G ₃₄	N ₂ ⁺ + N ₂ + M -> N ₄ ⁺ + M	5.0e-41	0	0		
G ₃₅	N ₄ ⁺ + O ₂ -> O ₂ ⁺ + N ₂ + N ₂	2.5e-16	0	0		3.51
G ₃₆	N ₂ ⁺ + O ₂ -> O ₂ ⁺ + N ₂	1.04e-15	-0.5	0		3.51
G ₃₇	O ₂ ⁺ + N ₂ + N ₂ -> O ₂ +N ₂ + N ₂	8.1e-38	-2.0	0.0		-
G ₃₈	O ₂ +N ₂ + N ₂ -> O ₂ ⁺ + N ₂ + N ₂	14.8	-5.3	2357.0		-
G ₃₉	O ₂ +N ₂ + O ₂ -> O ₂ ⁺ + N ₂	1.0e-15	0	0		-
G ₄₀	O ₂ ⁺ + N ₂ + M -> O ₄ ⁺ + M	2.03e-34	-3.2	0		-
G ₄₁	E + O ₂ + O ₂ -> O ₂ ⁺ + O ₂	6e-39	-1.0	0		0.43
G ₄₂	O ₂ ⁺ + O ₄ ⁺ -> O ₃ + O ₂ + O ₂	1e-13	0	0		11.64
G ₄₃	O ₂ ⁺ + O ₄ ⁺ + M -> O ₃ + O ₂ + O ₂ + M	3.12e-31	-2.5	0		11.64
G ₄₄	O ₂ ⁺ + O ₂ ⁺ + M -> O ₂ + O ₂ + M	3.12e-31	-2.5	0		11.64
G ₄₅	O ⁻ + O ₂ ⁺ -> O + O ₂	3.46e-12	-0.5	0		10.61
G ₄₆	N ₂ A + O ₂ -> N ₂ + O + O	1.7e-18	0	0		1.05
G ₄₇	N ₂ A + O ₂ -> N ₂ + O ₂ b1	7.5e-19	0	0		4.54
G ₄₈	N ₂ A + N ₂ A -> N ₂ + N ₂ B	7.7e-17	0	0		4.99
G ₄₉	N ₂ A + N ₂ A -> N ₂ + N ₂ C	1.6e-16	0	0		1.31
G ₅₀	N ₂ A + N ₂ -> N ₂ + N ₂ B	1.0e-16	0	1500.0		0.32
G ₅₁	N ₂ A + O -> N ₂ + O	3.0e-17	0	0		6.17
G ₅₂	N ₂ B + O ₂ -> N ₂ + O + O	3.0e-16	0	0		2.23
G ₅₃	N ₂ B + N ₂ -> N ₂ A + N ₂	1.0e-17	0	0		1.18
G ₅₄	N ₂ a1 + O ₂ -> N ₂ + O + O	2.8e-17	0	0		3.28
G ₅₅	N ₂ a1 + N ₂ -> N ₂ + N ₂	2.0e-19	0	0		8.4
G ₅₆	N ₂ C + O ₂ -> N ₂ + O + O	3.0e-16	0	0		5.91
G ₅₇	N ₂ C + N ₂ -> N ₂ a1 + N ₂	1.0e-17	0	0		2.63
G ₅₈	N ₂ C -> N ₂ B	3e7	0	0		-
G ₅₉	O ₂ [*] + O ₂ -> O ₂ a1 + O ₂	1.86e-19	0	0		3.52
G ₆₀	O ₂ ^{* + O₂ -> O₂b1 + O₂}	8.1e-20	0	0		2.87
G ₆₁	O ₂ ^{* + O₂ -> O₂ + O₂}	2.3e-20	0	0		4.5
G ₆₂	O ₂ ^{* + O -> O₂ + O}	5.0e-18	0	0		4.5
G ₆₃	O ₂ ^{* + O -> O₂a1 + O}	2.7e-18	0	0		3.52
G ₆₄	O ₂ ^{* + O -> O₂b1 + O}	1.35e-18	0	0		2.87

1 2 3 ***Simulation setup***

4
5 Computational domain and mesh characteristics are illustrated in Figure 3. An axisymmetric two-
6 dimensional domain was chosen for this study. Main features are the two concentric electrodes, a round-tip
7 anode (top electrode) and a flat top cathode (bottom electrode), the centerline, and outer boundaries away
8 from the electrode gap. Electrode profiles match the nominal dimensions that were measured in experiments.
9 The anode tip radius is 125 μm , and the cathode tip has a flat top surface with a diameter of 0.44 mm. The
10 inter-electrode tip-to-tip gap size is 5.2 mm and is fixed in all the simulations performed here. The
11 computational mesh is made of mixed triangle and quadrilateral cells. Small triangle cells are used at the
12 electrode surfaces to properly account for the electrode geometry. The triangle cells then transit to
13 quadrilateral cells with a fixed cell length (10 μm , i.e. the minimum cell size) in the central gap region
14 identified by the white rectangle in Figure 3. This is the region where the streamers are formed and
15 propagate. In regions away from the gap centerline, a progressively coarser triangle mesh is generated to
16 keep relatively low total cell counts ($\approx 80,000$), thereby reducing simulation time. The smallest cell size is
17 10 μm , which delivers a good compromise between accuracy and simulation time. The analysis of the
18 impact of mesh resolution on this type of simulations was performed in a previous study [18].
19
20
21
22
23
24
25
26
27



55 *Figure 3. Computational domain and mesh details*

The centerline features an axis boundary condition that ensures three-dimensional symmetry, with open surface symmetry boundaries at the outer edge of the domain. The electrode surfaces are treated as equipotential surfaces for the electrostatic potential solution and as solid surfaces with wall boundary processes for the species density and temperature equations. Raw profiles from the experiments (shown in Figure 2) are applied to the anode as voltage boundary condition.

The initial gas temperature is 343 K (corresponding to 70 °C), with the gas composed of 20.95% O₂ and 79.05% N₂ in volume fractions. The initial electron number density is set at 10⁹ m⁻³, which is also the default ground level for all the involved species other than O₂ and N₂. The initial electron number density has been found to significantly impact the time required for the streamer to emerge within the gap [17], also referred as to induction time. However, preliminary calculations not shown in this paper have confirmed this finding, but also shown that the streamer induction time does not affect the LTP-to-arc pressure threshold.

Finally, in order to resolve the dynamics of the nanosecond discharge, a fixed time step of 2x10⁻¹³ s was used. The total physical time simulated was about 150 ns depending on the specific operating conditions. For each of these conditions, simulations were carried out for as long as the applied voltage was high enough to impact the streamers characteristics.

As a summary, compared to previously published numerical and experimental work [18], the gap distance increased slightly (5.2 mm versus 5.0 mm), the cathode geometry changed (flat top versus round tip), and the concentration was pure desiccated air (versus a mixture of oxygen and nitrogen with the addition of small components that were not quantified). Also, several maximum voltage values were investigated (i.e. 10.3 kV, 14.4 kV, 19.2 kV, and 22.5 kV) and the LTP-to-arc transition for all of those voltage settings was calculated and validated against experiments. Furthermore, for the first time to the best of our knowledge, in this paper the experimental measurement of temperature and atomic oxygen in the proximity of the anode was targeted by simulations in order to deliver a quantitatively validated numerical methodology.

Results and discussion

Results will be illustrated according to the following order: first, the calibration of the model to match experimental data will be discussed, based on previous findings; next, the comparison with experimental data will be shown in a quantitative fashion, for both the LTP-to-arc transition and the plasma characteristics; finally, insight into the streamer propagation mechanisms as well as the post-discharge streamer properties will be provided; finally, additional considerations introducing future research studies will be provided.

Model calibration

Previous numerical studies performed at Argonne [18] showed that the transient plasma model is capable of matching the experimental observations in terms of streamers' behavior and appearance: higher pressure in the gap delivered slower, thinner streamers with higher tendency to branch. Also, the distribution of atomic oxygen and temperature seemed to qualitatively match corresponding images of electronically excited atomic oxygen after the discharge and schlieren images of density gradients from Sandia [14]. The main disagreement that was observed concerned the transition pressure threshold between the spark (arc) and glow (LTP) regimes. Simulations performed in [18] predicted such transition at a lower pressure with respect to experiments, i.e. 1.6 bar versus 2.2-2.8 bar.

However, some potential sources for uncertainty were identified in both the experiments (exact gas composition, electrode nominal geometry, and voltage measurements) and the simulations (initial electron seeding, electrode geometry irregularities, chemical kinetics). Preliminary numerical investigations (not shown) led to the conclusion that initial electron seeding and irregularities in the electrode geometry might affect the streamer induction time (i.e. the time from the beginning of the discharge that the streamers take to start propagating from the electrodes), but ultimately have no effect on the final prediction of the discharge regime, be it either spark or glow. Therefore, while experiments focused on accurately measuring the nominal geometry, simulations focused on tuning the chemistry to match the experiments.

Results on the model calibration are shown in

Table 4. It is worth noting that: 1) only the intermediate voltage conditions (14.4 kV and 19.2 kV) were evaluated for model calibration; 2) experiments are repeated a number of times and a probability number is provided as an output, while simulations will always fall in either one of the two regimes. The non-tuned model showed a discrepancy with respect the experiment of about 0.65 bar (for the 19.2 kV case), which is in line with previous results [18]. Tuning the electron collision frequency from the default multiplicative factor of $\xi_{v_E} = 1.0$ to $\xi_{v_E} = 0.3$ increased the LTP-to-arc transition pressure to better match the experiments.

Again, we note that this multiplicative factor accounts for model uncertainties associated with the collision cross section used in the description of the transport properties. More details about the tuning procedure is provided in the last section of the results.

Table 4. Comparison between experiments and modeling in terms of post-discharge regime

	EXPERIMENTS		MODELING (before tuning)	MODELING (after tuning)
V_{peak} (kV)	Arc probability 100% (Spark)	Arc probability 0% (Glow)	Transition from Spark (arc) to glow (LTP)	Transition from Spark (arc) to glow (LTP)
10.3	1.07	1.14		
14.4	1.33	1.45	Below 1.0 bar	Between 1.35 and 1.4 bar
19.2	1.69	1.86	Between 1.0 and 1.2 bar	Between 1.8 and 1.9 bar
22.5	2.87	3.27		

Validation against experiments

Once the model was calibrated, validation against experiments was performed. The first step was to extend the simulations to all the operating conditions evaluated in the paper. Figure 4 shows the comparison between experiments and modeling in terms of post-discharge regime for the entire experimental dataset. It is worth mentioning that simulations would not be able to capture the intermediate red region where a probability of arc between 0% and 100% was observed experimentally.

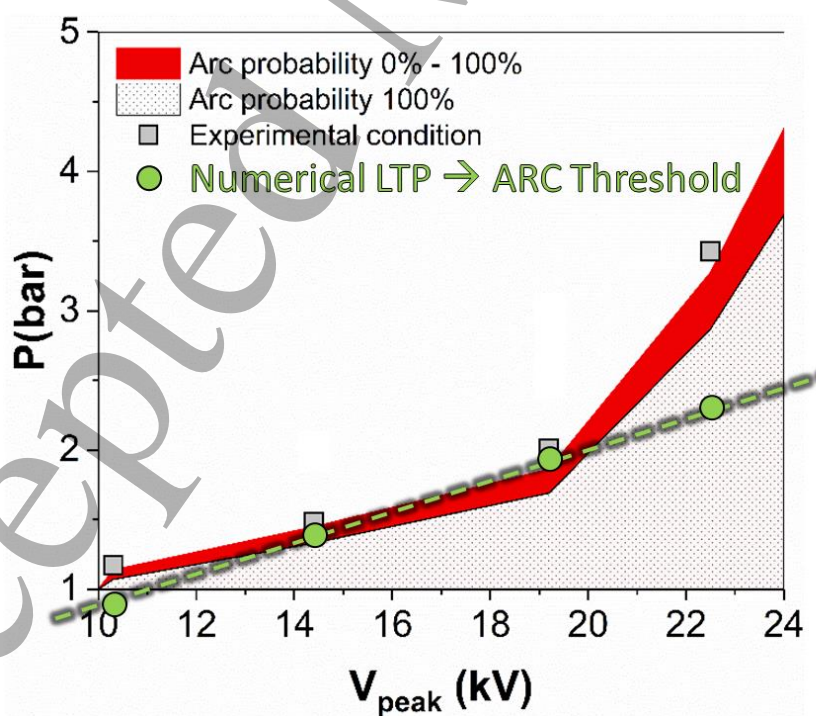


Figure 4. Comparison between experiments and simulations in term of LTP-to-arc transition

Overall, simulations do a good job reproducing the experiment results. The exception was for the lowest and highest voltage tested, which still show discrepancy (especially at the highest voltage value) between the observed and modeled breakdown limits. It is possible that the model is missing additional physics that becomes dominant at such higher voltage conditions (this is discussed further in the last section of the results). However, the linear trend captured by simulations over a relatively wide range of voltage values is justified by theoretical considerations. The post-discharge regime depends on the reduced electric field, E/N, and while the electric field E depends on the voltage, the number density is a linear function of pressure (temperature is constant in the cases analyzed in this paper). Therefore, in theory the linear trend makes adequate sense, and something else could contribute to deviate the experiments from the linear behavior.

Table 5 shows the comparison between experimental measurements and numerical calculations of the ground state of atomic oxygen and bulk gas temperature. Both measurements and calculations are performed at the same location in the proximity of the anode (shown in Figure 1), and at the same pressure value. The agreement between experimental and numerical data in Table 5 is good. To the authors' best knowledge, this is one-of-a-kind quantitative comparison performed in the LTP modeling literature. It can be concluded that a well-tuned model is capable of delivering accurate predictions of the relevant properties of transient plasmas.

Table 5. Comparison between experiments and simulations in terms of atomic oxygen (ground state) and temperature in the near-anode region

Test condition	Simulation		Experiment	
	O (1/cm ³)	T (K)	O (1/cm ³)	T (K)
14.4 kV, 1.5 bar	0.9 x 10 ¹⁸	770	1.3 x 10 ¹⁸	779
19.2 kV, 2.0 bar	1.8 x 10 ¹⁸	938	2.1 x 10 ¹⁸	1094

General description of the streamer discharge

This section aims at providing more insight into the streamer propagation process and post-discharge plasma characteristics. To this purpose, Figure 5 shows the evolution of the electron number density and reduced electric field E/N for both the arcing and non-arcing conditions calculated with a nominal voltage of 14.4 kV. It can be seen that at the threshold for glow-to-arc (spark) transitions even a small difference in the initial pressure value (1.35 bar versus 1.40 bar) can exhibit very different post-discharge plasma regimes. Indeed, the onset and propagation of the streamers is very similar and occurs only a bit faster (meaning that the process starts 1 ns earlier) for the lower pressure case. The entire process, including streamer propagation and connection, is consistently delayed by 1 ns at higher pressure. The only other difference is

that the induction of the negative streamer is not clearly visible for the higher pressure case (1.40 bar). However, at 87 ns and 88 ns respectively, it can be seen that both the positive and negative streamers have formed, have propagated in the gap, and have connected with each other. While visually the difference between the two pressure cases is minor, the post-discharge results are quite different.

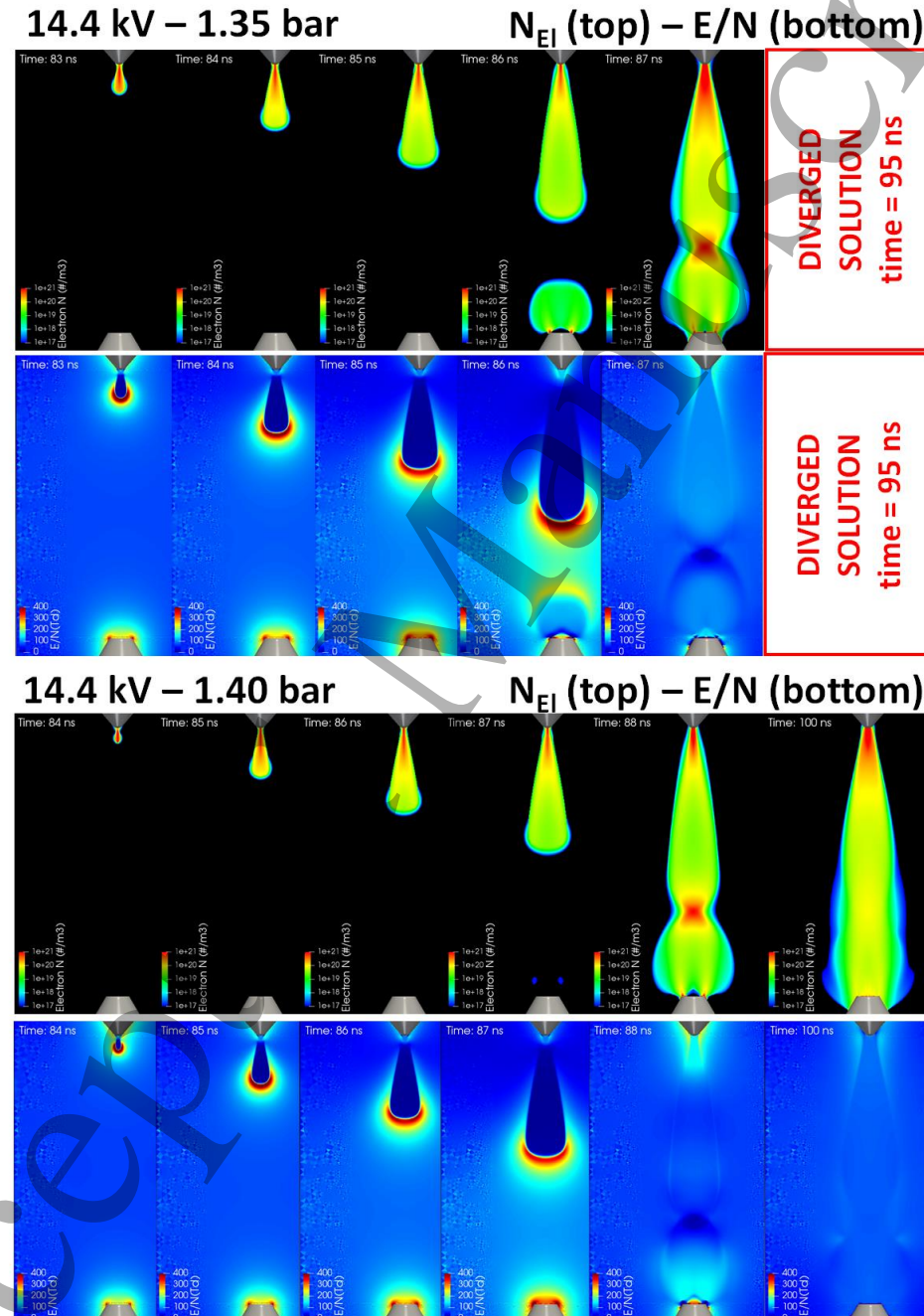


Figure 5. Streamer propagation mechanism in the spark (1.35 bar) and glow (1.40 bar) regimes for an applied peak voltage of 14.4 kV

Figure 5 shows that the solution for the lower pressure case diverged approximately 93 ns after the simulation start and is taken to be due to the onset of arcing (sparking) for which the non-equilibrium plasma formulation becomes mathematically too stiff to be properly resolved. Figure 6 shows the transient evolution of the discharge currents for the two cases. The lower pressure case is characterized by a steep increase in the electrical current at the time the positive and negative streamers connect to form a highly conducting channel in the entire gap. This increase in current corresponds to an exponential increase in the electron density, i.e. transition to arcing. As can be seen in the slightly higher pressure (1.40 bar) the increase of current is followed by a current drop while the plasma remains in an LTP glow state.

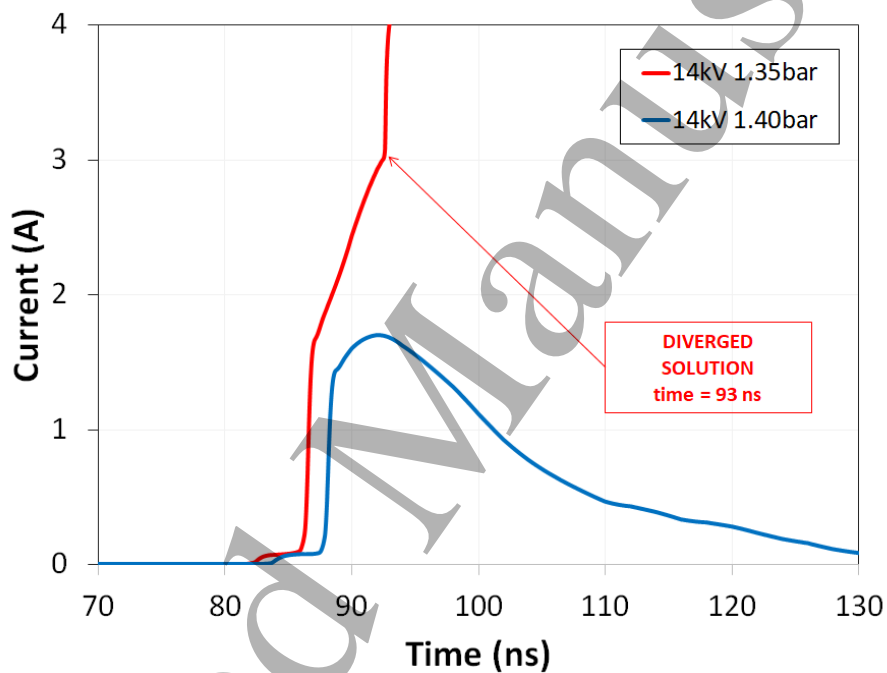


Figure 6. Electrical current profile for spark (1.35 bar) and glow (1.40 bar) regimes for an applied peak voltage of 14.4 kV

Figure 7 shows the thermal (bulk gas temperature) and chemical (ground state atomic oxygen) plasma characteristics at the end of the discharge, after the voltage has dropped to very low values. The above-arc pressure conditions (i.e. 1.40 bar and 1.90 bar) are shown for discharges with the peak voltages of 14.4 kV and 19.2 kV respectively. Higher pressure values show tendency to branch, which again matches experimental observations. In general, it must be highlighted here that the gas temperature is greater than the initial values, and actually reaches out fairly high (> 1000 K) values in the proximity of the anode. This location corresponds to the region where also the production of atomic oxygen is the highest.

It is worth noting that the geometry of the electrodes dictates where the highest temperature values and radical production are located. In the case of the geometry evaluated in this paper, the anode has a sharper

tip compared to the cathode flat top surface, therefore the streamer will generate and propagate first from the anode. Also, for the same reason, the local electric field enhancement will be larger in the proximity of the anode, resulting in higher temperature and production of active species. Overall, distribution of temperature and active species that trigger the ignition process at a later stage is what is needed to investigate LTP ignition processes. Once again it is shown in Figure 7 that the higher the pressure, the less uniform the plasma characteristics are (also due to increased branching), thus requiring multi-dimensional numerical tools for proper analysis.

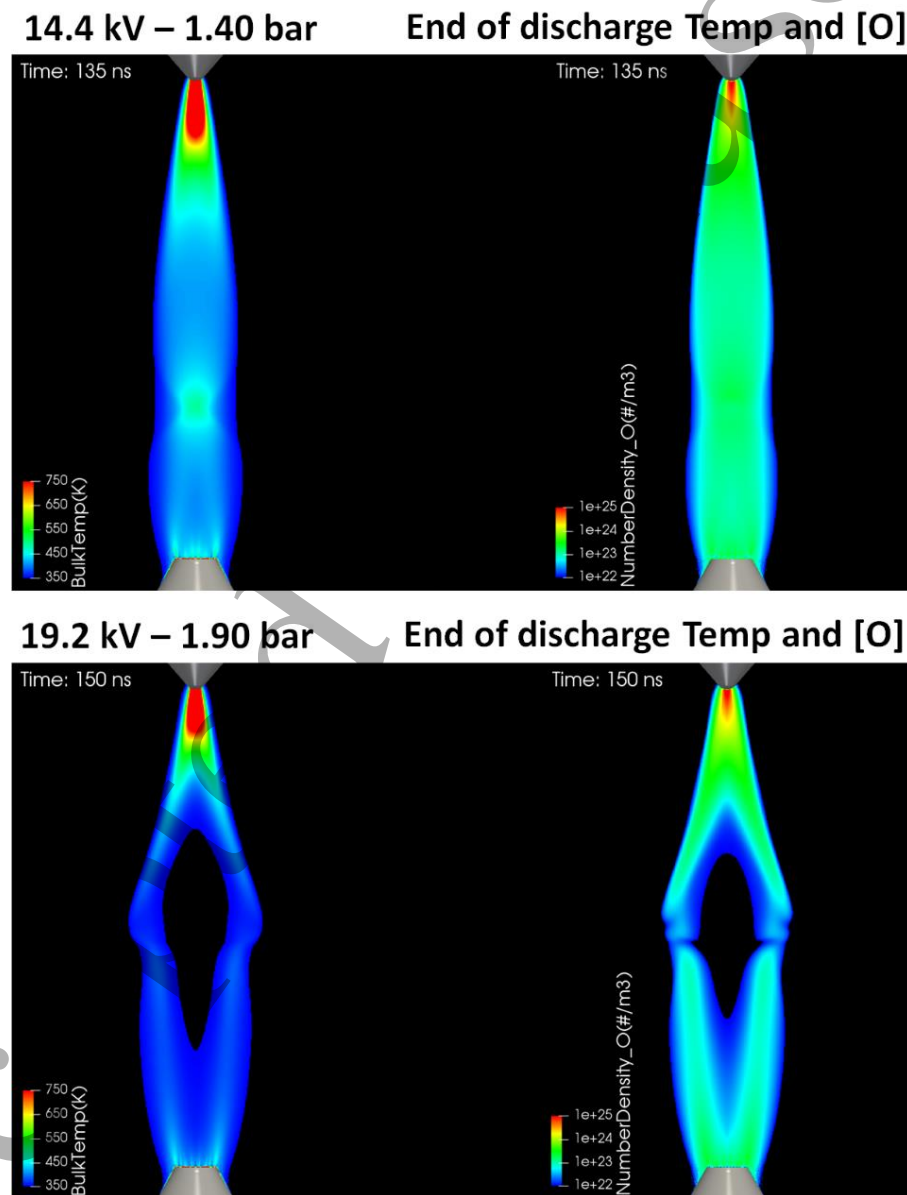


Figure 7. Thermal (Temperature) and chemical (atomic oxygen) plasma properties at the end of the discharge (main pulse) for 14.4kV and 19.2kV at near-arc conditions

1 2 3 ***Further considerations and future steps*** 4

5 The goals of this paper as defined in the introduction (i.e. improving the agreement between experiments
6 and modeling, and provide quantitative validation of plasma properties) were successfully met, yet margins
7 for potential improvement of the numerical methodology proposed in this study can be identified.
8
9

10 We have found that within the context of the non-equilibrium plasma fluid model the results are sensitive
11 to the electron collision frequency that enter the description of the electron transport properties. We have
12 used this as an effective tuning/calibration parameter for the model, justifying this based on the general
13 uncertainty that exists in determining the collision cross-section of the electrons in a complex chemical
14 environment under very high driving electric-field conditions. Other simulation parameters (in particular
15 the initial electron seeding and geometry irregularities) and their effect on the LTP-to-arc transition pressure
16 threshold need to be explored further, although preliminary studies delivered a negligible impact on the
17 post-discharge regime. Uncertainties associated with the plasma chemistry and in particular the cross
18 sections of electron-impact reactions (that are of most relevance to fast transient phenomena in streamers)
19 are a subject of ongoing studies by various investigators [28,29]. We note that, despite the many different
20 sources of model uncertainties, we have found that a single parameter, i.e. electron collision frequency,
21 provided an opportunity for fast calibration of the model to achieve good quantitative agreement with
22 experiments. This does not mean that the electron collision frequency is 70% wrong. The discrepancy
23 between the multiplier values 0.3 and 1.0 simply accounts with potentially other uncertainties that we still
24 have not explored. As an example, in the real case, flow and slow heating of the channel (the phase after
25 the streamer forms where the reduced electric field slowly builds up as the channel heats) are crucial physics
26 that should be taken into account. Coupling the flow physics and capturing gas channel heating and
27 relaxation could be important for more accurately predicting the transition and is another source of
28 uncertainty.
29
30

31 As far as the comparison between experiments and simulations shown in Figure 4 is concerned, it is
32 observed that the model calibration does not remove the discrepancy entirely, especially when a large range
33 of conditions are simulated. Furthermore, the role of voltage oscillations (ringing) and their impact on
34 plasma discharge and post-discharge ignition remains to be studied. Indeed, it was noticed that the voltage
35 oscillations after the main pulse were wider for the 22.5 kV nominal case with respect to the other conditions.
36
37

38 In general, the information provided by non-equilibrium plasma models are very valuable to evaluate the
39 LTP ignition mechanism. Specifically, the post-discharge plasma properties and also the impact of the post
40 discharge conditions on subsequent pulses, when the nanosecond pulsed discharge is operated in a multi-
41 pulse fashion can be studied readily. Ultimately, our research will focus on the LTP ignition mechanism
42
43

1
2
3 and a more comprehensive chemical scheme that can model the transition from LTP plasma into an actual
4 flame, to be used for modeling PAI applications.
5
6

7 Conclusions 8

9 A numerical methodology was used in this study to investigate the effect of nanosecond pulsed discharge
10 on the plasma characteristics, including the post-discharge regime and the thermal and chemical properties
11 of transient plasma in a glow (LTP) regime. Main conclusions are listed as follows:
12
13

- 14 • Previous numerical results were confirmed, in that an off-set of about 0.6 - 0.7 bar between
15 modeling and experiments was found when calculating the pressure value for the regime transition
16 from spark into glow. Simulations under-predicted the transition pressure value, consistently with
17 the previous study.
18
- 19 • Some experimental uncertainties, including gas composition and electrode geometries, were
20 removed as well as some numerical uncertainties, mainly concerning the initial (seeding) and
21 boundary (geometry tolerance) conditions.
22
- 23 • Rather than tuning all other possible sources of uncertainty, we chose to look at sensitivity to
24 electron collision frequency as a single tuning parameter. A calibrated model was capable of
25 reducing the gap between modeling and experiments and improve the numerical prediction of the
26 plasma regime on quantitative basis.
27
- 28 • While some discrepancies remained right at the boundaries of the experimental dataset (low and
29 high voltage conditions), the quantitative agreement between simulations and experiments in terms
30 of certain thermal (temperature) and chemical (atomic oxygen) plasma properties was good.
31
- 32 • The evaluation of the discharge in both glow and spark regime showed that the numerical tool used
33 in this study is capable of providing a comprehensive characterization of the two regimes'
34 boundaries, although it cannot fully handle simulations in the spark regime.
35
- 36 • Future studies will be looking at further improving the current numerical predictions and
37 transitioning into investigating the LTP ignition mechanism.
38

39 Acknowledgments 40

41 The submitted manuscript has been created by UChicago Argonne, LLC, Operator of Argonne National
42 Laboratory ("Argonne"). Argonne, a U.S. Department of Energy Office of Science laboratory, is operated
43 by UChicago Argonne, LLC under Contract DE-AC02-06CH11357.
44
45

under Contract No. DE-AC02-06CH11357. The U.S. Government retains for itself, and others acting on its behalf, a paid-up nonexclusive, irrevocable worldwide license in said article to reproduce, prepare derivative works, distribute copies to the public, and perform publicly and display publicly, by or on behalf of the Government.

This research is funded by DOE's Vehicle Technologies Program, Office of Energy Efficiency and Renewable Energy. The authors would like to express their gratitude to Gurpreet Singh, Mike Weismiller, and Leo Breton (retired), program managers at DOE, for their support. Numerical simulations were run on the Bebop Cluster at the LCRC facility, Argonne National Laboratory.

References

- [1] Briggs, T., Alger, T., and Mangold, B., "Advanced Ignition Systems Evaluations for High-Dilution SI Engines," SAE Int. J. Engines 7(4):1802-1807, 2014.
- [2] Sevik, J., Wallner, T., Pamminger, M., Scarcelli, R., et al., "Extending Lean and Exhaust Gas Recirculation-Dilute Operating Limits of a Modern Gasoline Direct-Injection Engine Using a Low-Energy Transient Plasma Ignition System," J. Eng. Gas Turbines Power 138(11):112807, 2016.
- [3] Sjöberg, M., Zeng, W., Singleton, D., Sanders, J.M., et al., "Combined Effects of Multi-Pulse Transient Plasma Ignition and Intake Heating on Lean Limits of Well-Mixed E85 DISI Engine Operation," SAE Int. J. Engines 7(4):1781–1801, 2014.
- [4] Starikovskaia, S.M., "Plasma assisted ignition and combustion," J. Phys. Appl. Phys. 39(16):R265, 2006.
- [5] Starikovskaia, S.M., "Plasma-assisted ignition and combustion: nanosecond discharges and development of kinetic mechanisms," J. Phys. Appl. Phys. 47(35):353001, 2014.
- [6] Wolk, B., DeFilippo, A., Chen, J.-Y., Dibble, R., et al., "Enhancement of flame development by microwave-assisted spark ignition in constant volume combustion chamber," Combust. Flame 160(7):1225–1234, 2013, doi:10.1016/j.combustflame.2013.02.004
- [7] Nishiyama, A. and Ikeda, Y., "Improvement of Lean Limit and Fuel Consumption Using Microwave Plasma Ignition Technology," 2012, doi:10.4271/2012-01-1139
- [8] Chintala, N., Bao, A., Lou, G., and Adamovich, I.V., "Measurements of combustion efficiency in nonequilibrium RF plasma-ignited flows," Combust. Flame 144(4):744–756, 2006, doi:10.1016/j.combustflame.2005.08.040
- [9] Hampe, C., Kubach, H., Spicher, U., Rixecker, G., et al., "Investigations of Ignition Processes Using High Frequency Ignition," 2013, doi:10.4271/2013-01-1633
- [10] D Singleton et al. "The role of non-thermal transient plasma for enhanced flame ignition in C₂H₄-air", 2011 J. Phys. D: Appl. Phys. 44 022001.
- [11] S J Pendleton et al. "The production and evolution of atomic oxygen in the afterglow of streamer discharge in atmospheric pressure fuel/air mixtures" 2013 J. Phys. D: Appl. Phys. 46 305202.
- [12] Pai, D.Z., Lacoste, D.A., and Laux, C.O., "Transitions between corona, glow, and spark regimes of nanosecond repetitively pulsed discharges in air at atmospheric pressure," J. Appl. Phys. 107(9):093303, 2010, doi:10.1063/1.3309758.
- [13] Wolk, B. and Ekoto, I., "Calorimetry and Atomic Oxygen Laser-Induced Fluorescence of Pulsed Nanosecond Discharges at Above-Atmospheric Pressures," Ignition Systems for Gasoline Engines, Springer International Publishing, Cham: 169–189, 2017.

- [14] Wolk, B.M. and Ekoto, I., "Calorimetry and Imaging of Plasma Produced by a Pulsed Nanosecond Discharge Igniter in EGR Gases at Engine-Relevant Densities," SAE Int. J. Engines 10(3), 2017.
- [15] Ju, Y. and Sun, W., "Plasma assisted combustion: Dynamics and chemistry," Prog. Energy Combust. Sci. 48(0):21–83, 2015.
- [16] Tholin, F. and Bourdon, A., "Influence of temperature on the glow regime of a discharge in air at atmospheric pressure between two point electrodes," J. Phys. Appl. Phys. 44(38):385203, 2011.
- [17] Tholin, F. and Bourdon, A., "Simulation of the stable 'quasi-periodic' glow regime of a nanosecond repetitively pulsed discharge in air at atmospheric pressure," Plasma Sources Sci. Technol. 22(4):045014, 2013.
- [18] Scarcelli, R., Zhang, A., Wallner, T., Breden, D. et al., "Multi-dimensional Modeling of Non-equilibrium Plasma for Automotive Applications," SAE Technical Paper 2018-01-0198, 2018, <https://doi.org/10.4271/2018-01-0198>.
- [19] VizGlow Theory Manual, 2016, <http://esgeetech.com/>
- [20] Breden, D., Raja, L.L., Idicheria, C.A., Najt, P.M., et al., "A numerical study of high-pressure non-equilibrium streamers for combustion ignition application," J. Appl. Phys. 114(8):083302, 2013.
- [21] Pancheshnyi, S., Nudnova, M., and Starikovskii, A., "Development of a cathode-directed streamer discharge in air at different pressures: Experiment and comparison with direct numerical simulation," Phys. Rev. E 71(1), 2005, doi:10.1103/PhysRevE.71.016407
- [22] Kossyi, I.A., Kostinsky, A.Y., Matveyev, A.A., and Silakov, V.P., "Kinetic scheme of the non-equilibrium discharge in nitrogen-oxygen mixtures," Plasma Sources Sci. Technol. 1(3):207, 1992
- [23] Aleksandrov, N., Kindysheva, S., Kukaev, E., Starikovskaya, S., Starikovskii, A., "Simulation of the Ignition of a Methane-Air Mixture by a High Voltage Nanosecond Discharge", Plasma Physics Reports, Vol. 25, No. 10, pp. 867-882, 2009
- [24] Hagelaar, G.J.M. and Pitchford, L.C., "Solving the Boltzmann equation to obtain electron transport coefficients and rate coefficients for fluid models," Plasma Sources Sci. Technol. 14(4):722–733, 2005, doi:10.1088/0963-0252/14/4/011
- [25] Bourdon, A., Pasko, V.P., Liu, N.Y., Celestin, S., Segur, P. and Marode, E., "Efficient models for photoionization produced by non-thermal gas discharges in air based on radiative transfer and the Helmholtz equations" Plasma Sources Sci. Technol. 16(3):656–678, 2007, doi:10.1088/0963-0252/16/3/026
- [26] Breden, D., Miki, K. and Raja, L.L., "Self-consistent two-dimensional modeling of cold atmospheric-pressure plasma jets/bullets" Plasma Sources Sci. Technol. 21(3):034011(13pp), 2012, doi:10.1088/0963-0252/21/3/034011
- [27] Zheleznyak, M.B., Mnatsakanyan, A.K. and Sizykh, S.V., "Photoionization of nitrogen and oxygen mixtures by radiation from a gas discharge", High Temp. 20(3), 357-62
- [28] Kieffer, L.J., Dunn, G.H, "Electron Impact Ionization Cross_Section Data for Atoms, Atomic Ions, and Diatomic Molecules: I. Experimental Data", Reviews of Modern Physics, 38(1):1-35, 1966.
- [29] Pancheshnyi, S., Biagi, S., Bordage, M.C., Hagelaar, G.J.M., et al." The LXCat project: Electron scattering cross sections and swarm parameters for low temperature plasma modeling", Chem. Phys. 398 (2012) 148–153, <https://doi.org/10.1016/j.chemphys.2011.04.020>.